

# Electron Temperatures and Free-Electron Energy Distributions of Nebulae from C II Dielectronic Recombination Lines

Peter J. Storey<sup>1\*</sup> and Taha Sochi<sup>1\*†</sup>

<sup>1</sup>*University College London, Department of Physics and Astronomy, Gower Street, London, WC1E 6BT*

Accepted XXX. Received XXX; in original form XXX

## ABSTRACT

A recently generated theoretical line list of C II dielectronic recombination lines together with observational data gathered from the literature is used to investigate the electron temperature in a range of astronomical objects, mainly planetary nebulae. The electron temperature is obtained by a least-squares optimisation using all the reliable observed lines in each object. In addition, the subset of lines arising directly from autoionising states is used to directly determine the free-electron energy distribution which is then compared with various theoretical possibilities. The method described here can potentially determine whether there are departures from Maxwell-Boltzmann distributions in some nebulae, as has been recently proposed. Using published observations of the three planetary nebulae where the relevant lines are recorded, we find that the data are best matched by Maxwell-Boltzmann distributions but that the uncertainties are sufficiently large at present that  $\kappa$ -distributions or two-component nebular models are not excluded.

**Key words:** planetary nebulae; general – atomic processes – methods: numerical – radiation mechanisms: general – ISM: abundances – stars: kinematics and dynamics.

## 1 INTRODUCTION

Recombination plays an essential role in the physical processes that occur in nebulae, the principal electron-ion recombination processes being Radiative Recombination (RR) and Dielectronic Recombination (DR). Recombination of an electron and ion may take place through a background continuum known as radiative recombination, or through a resonant recombination process involving doubly-excited states known as dielectronic recombination. The latter can lead either to autoionisation, which is a radiationless transition to a lower state with the ejection of a free electron, or to stabilisation by radiative decay to a lower bound state, possibly the ground state, with a bound electron. The RR and DR processes are closely linked and the difference between them may therefore be described as artificial; quantum mechanically they are indistinguishable.

In section 2 of this paper we determine an electron temperature from dielectronic recombination lines of C<sup>+</sup> in the spectra of a number of astronomical objects, mainly planetary nebulae, using a least squares optimisation method with theoretical data obtained from the recently-computed theo-

retical line list, SS1, of Sochi & Storey (2012) and astronomical data gathered from the literature. The theoretical list was generated using the **R**-matrix (Berrington *et al* 1995), Autostructure<sup>1</sup> (Eissner *et al* 1974; Nussbaumer & Storey 1978) and Emissivity (Sochi 2010) codes with an intermediate coupling scheme where the lines are produced by DR processes originating from low-lying autoionising states with subsequent cascade decays. The method of formation of DR lines is particularly simple, often only requiring the radiative probability of the transition in question and experimentally known properties, the energy and statistical weight of the autoionising upper state. Even in more complex cases, only autoionisation probabilities are required in addition. This can be compared with the complex recombination and collisional-radiative processes involved in obtaining effective recombination coefficients for transitions between low-lying ionic states (e.g. Davey *et al* (2000)). Determining electron temperatures from DR lines can therefore provide valuable evidence about the temperature structure of photoionised nebulae.

There is a long-standing puzzle in the physics of planetary nebulae involving the discrepancy between electron

\* E-mail: pjs@star.ucl.ac.uk (PJS).

† E-mail: t.sochi@ucl.ac.uk (TMS). Corresponding author.

<sup>1</sup> See Badnell: Autostructure write-up on WWW. URL: [amdpp.phys.strath.ac.uk/autos/ver/WRITEUP](http://amdpp.phys.strath.ac.uk/autos/ver/WRITEUP).

temperatures and ionic abundances derived from optical recombination lines (ORLs) and collisionally excited forbidden lines (CELs). Although the forbidden lines are much stronger than the recombination lines, they are highly dependent on temperature, making abundance determinations potentially uncertain. On the other hand, the recombination lines are weak and prone to blending and can be easily contaminated by radiation from other excitation processes such as fluorescence. Despite all these differences, there is a common feature between the results obtained from these lines; that is for all the atomic species investigated so far (mainly from the second row of the periodic table such as C, N, O and Ne) the forbidden lines in planetary nebulae normally produce lower ionic abundances than the corresponding values obtained from the recombination lines. The ratio of the ORL to the CEL abundances, the so-called abundance discrepancy factor or ADF, is case dependent and can be a factor of 30 or even more. This has cast some doubt on the validity of the previously accepted CELs analysis results, although the stability of CEL abundances and the wide variations in ORL abundances between objects suggest that we should seek the solution to the problem in the physics or origin of the ORLs. The abundance problem appears to be correlated to the differences between the temperatures obtained from the Balmer jump of H I and that from the collisionally-excited forbidden lines where the latter is systematically higher than the former (Kholtygin 1998; Liu 2002; Tsamis *et al* 2007). In fact, obtaining higher electron temperatures from forbidden lines than those deduced from recombination lines is a general trend in nebular studies.

Several explanations have been proposed to justify these discrepancies individually or collectively, though no one seems to be satisfactory or universally accepted. One explanation is the sensitivity of the collisionally-excited lines to temperature and structure fluctuations where these fluctuations within the nebular structure result in systematic underestimation of the heavy element abundances deduced from the forbidden lines. The existence of knots depleted of hydrogen with high heavy element contents within the nebular gas has been proposed as a possible reason for these fluctuations and subsequent implications. The temperature inside these knots of high metallicity, and hence high opacity to stellar ultraviolet emissions and large cooling rates, is expected to be too low for efficient production of forbidden lines though it is still sufficiently high for the emission of recombination lines. Consequently, the recombination and collisional lines originate in different regions of the nebular gas with different elemental abundances and different temperatures. However, the presence of such knots in most or all planetary nebulae, as would be required to explain the systematic nature of the observations, has not been confirmed observationally (Liu *et al* 1995; Garnett & Dinerstein 2001; Tsamis *et al* 2003; Liu *et al* 2004).

In a recent paper by Nicholls *et al* (2012) it is suggested that this long-standing problem in planetary nebulae and H II regions could arise from the departure of the electron energy distribution from the presumed Maxwell-Boltzmann equilibrium condition, and that it can be resolved by assuming a  $\kappa$ -distribution for the electron energy following a method used in solar data analysis. The electron energy distribution will be the subject of section 4 where we consider only lines originating from resonance states, that is free-free

(FF) and free-bound (FB) transitions. We obtain a direct sampling of the electron energy distribution from the observational de-reddened flux and the theoretically-obtained parameters such as the departure coefficients of the involved autoionising states and the radiative probabilities of these transitions.

## 2 METHOD OF ELECTRON TEMPERATURE INVESTIGATION

### 2.1 Theory

As indicated already, the theoretical data of the C II dielectronic recombination transitions and subsequent cascade decay are obtained from the SS1 line list of Sochi & Storey (2012) which consists of 6187 optically-allowed transitions with their associated data such as emissivity and effective recombination coefficients. The autoionising states involved in the transitions of this list consist of 64 resonances belonging to 11 symmetries ( $J = 1, 3, 5, 7, 9, 11$  half even and  $J = 1, 3, 5, 7, 9$  half odd) which are all the resonances above the threshold of  $C^{2+} 1s^2 2s^2 1S^e$  with a principal quantum number  $n < 5$  for the combined electron. These include 61 theoretically-found resonances by the **K**-matrix method (Sochi & Storey 2012) plus 3 experimental ones which could not be found due to their very narrow width. The bound states involved in these transitions comprise 150 energy levels belonging to 11 symmetries ( $J = 1, 3, 5, 7, 9$  half even and  $J = 1, 3, 5, 7, 9, 11$  half odd). These include 142 theoretically found by **R**-matrix, which are all the bound states with effective quantum number between 0.1-13 for the outer electron and  $0 \leq l \leq 5$ , plus 8 experimental top states which are the levels of the  $1s^2 2s 2p(^3P^o) 3d\ ^4F^o$  and  $^4D^o$  terms.

The theoretical and computational backgrounds for the atomic transition calculations including the emissivity thermodynamic model are given in Sochi (2010) and Sochi & Storey (2012). The calculations were performed using an elaborate  $C^{2+}$  ionic target in the intermediate coupling scheme. The list has also been validated by various tests including comparison to literature data related to autoionisation and radiative transition probabilities and effective dielectronic recombination coefficients. The theoretical parameters for the bound and resonance states were also compared to the available experimental data from the National Institute of Standards and Technology<sup>2</sup> and found to agree very well both in energy levels and in fine structure splitting.

Processes other than dielectronic recombination have not been considered in the atomic scattering and transition model of the SS1 list, so the results of SS1 are incomplete for states likely to be populated by radiative recombination or collisional excitation and de-excitation. Any transition in which the upper state has an excited ion core (usually  $2s 2p(^3P^o)$ ) will have negligible population by radiative recombination in typical nebular conditions and is therefore well represented by only dielectronic recombination and subsequent cascade processes. This includes all free-free and free-bound transitions plus those bound-bound transitions involving excited ion core states.

However, for the determination of temperature we also

<sup>2</sup> URL: [www.nist.gov](http://www.nist.gov).

include the 4f–3d transition,  $\lambda 4267 \text{ \AA}$ , which is the strongest optical C II recombination line and is populated almost exclusively by radiative recombination. As discussed above, the formation mechanism of the dielectronic lines is very simple while  $\lambda 4267$  lies at the bottom of a complex cascade process and our analysis provides a way, in some cases at least, of testing and validating the results obtained from  $\lambda 4267 \text{ \AA}$  and other low-lying transitions. For example, the possibility of the existence of some unknown mechanism that overpopulates the levels of the upper state of  $\lambda 4267$  transition causing the enhancement of the ORL abundance may be ruled out if the results with  $\lambda 4267$  are consistent with those obtained without  $\lambda 4267$ .

For  $\lambda 4267$ , recombination coefficients were taken from case B of Davey *et al* (2000). These were obtained within a more comprehensive theory that includes radiative and dielectronic recombination and all relevant collisional processes. They were obtained in LS-coupling rather than intermediate coupling but the coupling scheme should not significantly affect this transition.

## 2.2 Observational data

We carried out a search for C II recombination line data in the literature in which over 140 data sets related mainly to planetary nebulae were catalogued. All data sets that comprise only bound-bound transitions with no doubly-excited core upper state were removed. The remaining data sets were subjected to a refinement process in which the flux of all the observational lines in each data set were normalised to the flux of a reference observational line in the set, which is usually chosen as the brightest and most reliable, while the emissivity of all the theoretical lines in the set were normalised to the emissivity of the corresponding theoretical line. The ratio of the normalised observed flux to the normalised theoretical emissivity of each line were then plotted on common graphs as a function of temperature on log-linear scales. A sample of these graphs is presented in Figure 4 for the planetary nebula NGC 5315. All lines that did not approach the ratio of the reference line within an arbitrarily-chosen factor of 3 were eliminated. The arbitrary factor of 3 was chosen as an appropriate limit considering practical factors that contribute to errors in the collection of observational data. The refinement process also involved the utilisation of graphs in which the ratio of theoretical emissivity to observational flux of all lines in a certain data set was plotted on a single graph as a function of electron temperature. A sample of these graphs is shown in Figure 1.

Some lines were also eliminated for various reasons related mainly to an established or suspected misidentification of the line or its intensity. For example, the wavelength of the alleged C II line may not match with any known theoretical transition. Also, the absence of a strong line in the observational data associated with the presence of a much weaker line with no obvious reason casts doubt on the identification of the weaker line. The line may also be eliminated because its intensity ratio relative to another well-established line does not comply with the ratio obtained from theory. A very few lines were also out of the wavelength range of our line list and hence were eliminated due to lack of theoretical emissivity data.

The selected refined data sets were then subjected to a

least squares optimisation procedure which is outlined in the following section. It should be remarked that the observed flux used in the least squares procedure is the de-reddened flux obtained by correcting for extinction and other sources of error as stated by the data source and not the raw flux data. Therefore, there should be no ambiguity when we use ‘observed’ flux in the following sections.

## 2.3 Least Squares Minimisation

In our least squares calculations we use a single fitting parameter, which is the electron temperature, while the observations are the flux data of the C II recombination lines that we obtained from the literature. All blended C II lines in the observational list are combined by considering them as a single line with a single flux, while C II lines blended with non-C II lines are eliminated. To compare the theoretical emissivity to the observational flux, the theoretical emissivity of each line is normalised to the total theoretical emissivity of all the lines involved in the least squares procedure, while the observational flux of that line is normalised to the total observational flux of these lines. The normalised theoretical emissivities corresponding to a particular observational flux are added when the observational flux is given for a whole multiplet.

The  $\chi^2$  defined by the following equation

$$\chi^2 = \sum_{i=1}^N \frac{(I_i^{no} - \varepsilon_i^{nt})^2}{\eta \sigma_{I_i^{no}}^2} \quad (1)$$

is computed, where  $i$  is an index running over all the  $N$  lines involved in the least squares procedure,  $I_i^{no}$  and  $\varepsilon_i^{nt}$  are the normalised observational flux and normalised theoretical emissivity of line  $i$  respectively,  $\eta$  is the number of degrees of freedom, and  $\sigma_{I_i^{no}}^2$  is the variance of  $I_i^{no}$ . This variance is computed from formulae given in Sochi (2012). For the data sets with given observational errors the reported errors were used while for the data sets with no reported error a Poisson distribution was assumed and the error on the observed flux was assumed to be proportional to the square root of the flux. In some data sets, the observational error was given for some lines only, and hence the average of the given errors was assigned to the missing ones. In some cases when the reported error was unrealistically small resulting in large  $\chi^2$ , the  $\chi^2$  curve was scaled to unity at the minimum to obtain a more realistic error estimate.

The temperature of the object is then identified from its value at the minimum  $\chi^2$ , while the confidence interval is identified from the values of the temperature corresponding to the values of  $\chi_{\min}^2 \pm 1$  on the lower and upper sides. In some cases, the  $\chi^2$  curve was too shallow on one side and hence it resulted in a broad confidence interval on that side.

In the following section we present results for those objects where there were sufficient adequate observations to derive a temperature.

## 3 DERIVED TEMPERATURES

In this section we present the astronomical objects that have been investigated. The objects are mainly planetary nebulae and the physical parameter of interest is the electron

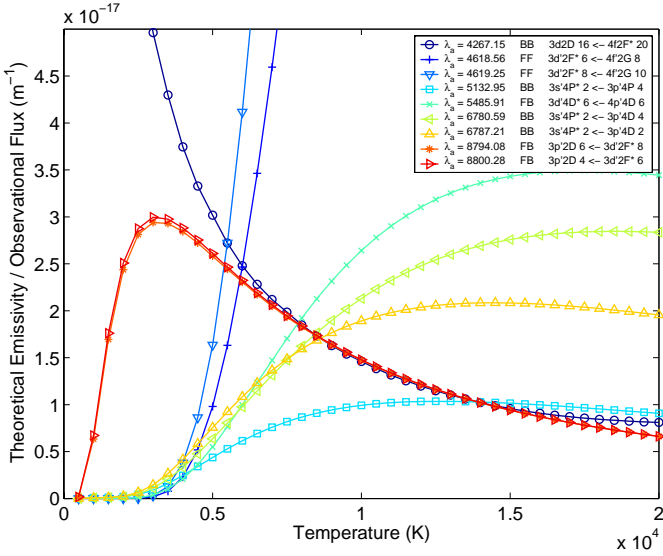


**Figure 1.** The ratio of theoretical emissivity to observational flux as a function of temperature for the selected C II lines from the NGC 7009 spectra of Fang & Liu (2011).

temperature of the line emitting regions. We also include three objects which are not planetary nebulae for comparison, where similar techniques have been used in the past. The theoretical and observational data for the transitions used in this investigation are given in Tables 1 and 2.

### 3.1 NGC 7009

NGC 7009 is a bright planetary nebula which has a double-ringed complex spatial structure with a rich recombination spectrum and a relatively large ADF. The observational data for this object were obtained from Fang & Liu (2011) where 9 lines, listed in Table 2, were chosen following the selection process. In Figure 1 the ratio of theoretical emissivity to observational flux is plotted against electron temperature on a linear-linear graph for these lines. If there were no errors in the observational fluxes or theoretical emissivities and the nebula was at a single uniform temperature, these curves would all intersect at the same temperature.

The  $\chi^2$  graphs, with and without  $\lambda 4267$ , are given in Figures 2 and 3. As seen, The first indicates a temperature of about 5800 K while the second a temperature of about 5500 K, which are in good agreement. We note also that in Figure 1 the curves for  $\lambda 4267$  and the DR doublet  $\lambda\lambda 8794, 8800 \text{ \AA}$  show very good agreement for  $T > 8000 \text{ K}$ . This indicates both that the theoretical emissivities of these lines are entirely consistent and also that the observational data for this object for these three lines are accurate.

In Table 3 we list electron temperatures from the cited literature derived from a range of ions and three types of spectral features: CELs, ORLs and the Balmer and Paschen discontinuities. As can be seen, the values that we obtained here are in a broad agreement with the temperature obtained from several recombination lines. The lower electron temperature from optical recombination lines compared to the values obtained from collisionally-excited lines is consistent with the trend of the discrepancy between the abun-

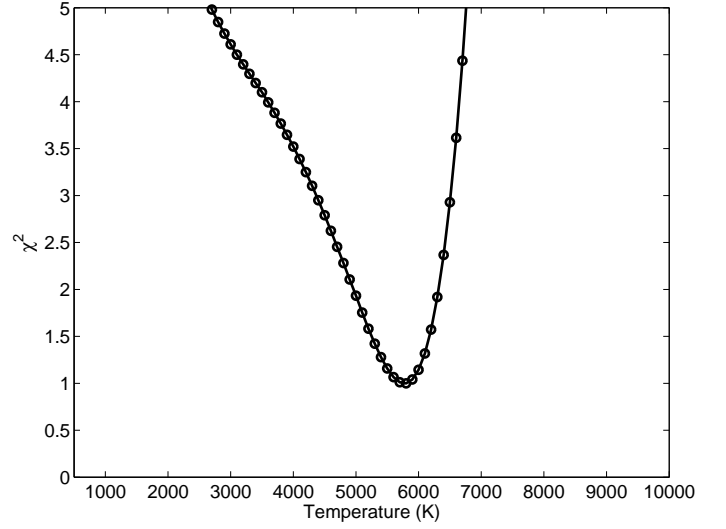


**Figure 2.** Temperature dependence of  $\chi^2$  for NGC 7009 with the inclusion of line  $\lambda 4267$ , where  $T = 5800 \text{ K}$  at  $\chi^2_{\min}$  with a confidence interval between 4961 – 6318 K.

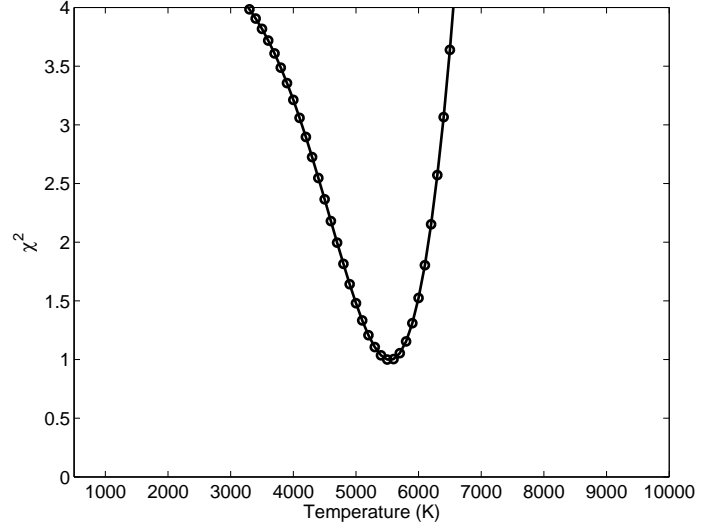


**Figure 3.** Temperature dependence of  $\chi^2$  for NGC 7009 with the exclusion of line  $\lambda 4267$ , where  $T = 5500 \text{ K}$  at  $\chi^2_{\min}$  with a confidence interval between 4697 – 6156 K.

dance and temperature results of ORL and CEL (higher ORL abundance and lower electron temperature as compared to the CEL abundance and temperature). If this discrepancy is caused by departures from a Maxwell-Boltzmann distribution by the free electrons, we might expect objects with the largest ADF to show the largest departures, so we also list ADF values from the literature in Table 3. NGC 7009 has the largest ADF of the objects in our sample of planetary nebulae. We discuss its electron energy distribution in Sec 4.

### 3.2 NGC 5315

NGC 5315 is a young dense planetary nebula in the southern constellation Circinus located at a distance of about 2.6 kpc

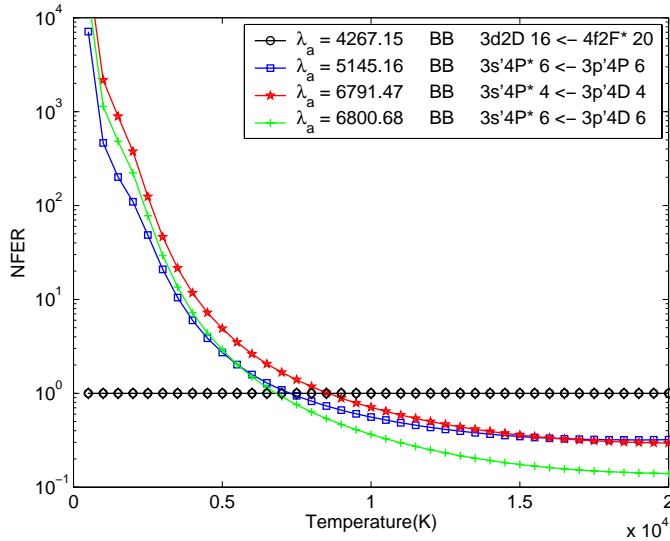


**Figure 4.** Ratio of normalised observed flux to normalised theoretical emissivity (NFER) versus temperature on log-linear scales for the planetary nebula NGC 5315.

with an interesting complex flower shape appearance. The observational data, which consist of 4 selected lines indicated in Table 2, were obtained from Peimbert *et al* (2004). Figure 4 displays the ratio of the normalised observed flux to the normalised theoretical emissivity versus electron temperature for these lines. Our  $\chi^2$  calculations, with and without line  $\lambda 4267$ , indicate  $T \simeq 7400$  K and  $T \simeq 6500$  K respectively. Table 3 presents some values of the electron temperature of NGC 5315 as reported in the cited literature. Again, the temperature is lower than that derived from the collisionally-excited lines.

### 3.3 NGC 7027

NGC 7027 is a compact, bright, young, high excitation planetary nebula with one of the hottest central stars known for a PN. Two observational data sets related to NGC 7027 were investigated: one obtained from Baluteau *et al* (1995), and the other obtained from Zhang *et al* (2005). Eight lines, listed in Table 2, were selected from Baluteau *et al*. The least squares optimisation of these lines indicate  $T \simeq 11100$  K, in good agreement with values obtained by other researchers; a sample of which is presented in Table 3. In the case of Zhang *et al*, 20 lines, given in Table 2, were chosen. The results of least squares, with and without line  $\lambda 4267$ , indicate  $T \simeq 12500$  K and  $T \simeq 12000$  K respectively.

### 3.4 IC 418

IC 418 is a bright, young, carbon-enhanced, low-excitation, highly symmetric planetary nebula with apparent ring structure located at a distance of about 0.6 kpc in the constellation Lepus. Our observational data on IC 418 come from Sharpee *et al* (2003) where 22 lines, presented in Table 2, were selected for least squares minimisation. The  $\chi^2$  plots, with and without line  $\lambda 4267$ , minimise at  $T \simeq 8700$  K and  $T \simeq 7700$  K respectively.

### 3.5 NGC 2867

NGC 2867 is a compact planetary nebula with comparatively small size and fairly strong surface brightness located at a distance of about 0.5 kpc in the southern constellation Carina. The observational data of this object were obtained from García-Rojas *et al* (2009) where two knots have been studied: one labelled NGC 2867-1 and the other NGC 2867-2. Two lines, given in Table 2, were selected for the optimisation process. The NGC 2867-1 result indicates  $T \simeq 14300$  K while NGC 2867-2 result indicates  $T \simeq 16000$  K. The difference in temperature value may be caused by the difference in the physical conditions of the two knots. Table 3 presents electron temperatures derived in previous works from transitions of different species. As seen, our values are significantly higher than most of the values reported in the literature. However, this may be explained by the complex structure of this nebula and the possibility of different lines being originating from different regions with very different physical conditions.

### 3.6 DQ Herculis 1934

This is a peculiar old classical galactic nova originating from an accreting cataclysmic variable binary system which apparently consists of a white and a red dwarf. Our observational data of this object were obtained from Ferland *et al* (1984) where 2 lines, given in Table 2, were chosen for least squares. The result indicates  $T \simeq 1600$  K, in very good agreement with some values reported in the literature (refer to Table 2) notably those of Smits (1991) and Davey (1995) which are also derived from C II recombination lines. The higher temperatures in the literature may belong to the hot inner disk region, rather than the cool outer shell, where much higher temperatures have been derived.

It should be remarked that the use of  $\lambda 1335$  Å line is a second exception (the first is  $\lambda 4267$  Å) to our rule of using the BB transitions only if the upper state has a doubly-excited core. The upper state of the  $\lambda 1335$  transition is  $1s^2 2s 2p^2$  which is connected to the  $C^{2+} 1s^2 2s^2$  continuum and  $1s^2 2s^2 nl$  Rydberg states by two-electron radiative processes which are usually very weak. Hence excitation of  $\lambda 1335$  Å by direct radiative recombination can be neglected.

### 3.7 CPD - 56°8032

CPD - 56°8032 is a cool late-type Wolf-Rayet star that is usually classified as WC10 or WC11. The star, which is located at about 1.3-1.5 kpc, is surrounded by a young planetary nebula with complex visible structure. Here, we try to infer the electron temperature of the stellar nebular wind surrounding CPD - 56°8032. The observational data of this object were obtained from De Marco *et al* (1997) where 13 lines, given in Table 2, were extracted following a selection process. The  $\chi^2$  plot indicates  $T \simeq 17300$  K. This agrees, within the reported error bars, with the temperature of De Marco *et al* (De Marco 1996; De Marco *et al* 1996) who deduced a value of  $18500 \pm 1500$  K for this object using a similar least squares approach. Our value also agrees reasonably with some of the values reported in the literature; a sample of which is given in Table 3.

### 3.8 He 2-113

He 2-113 is another late-type WC10 Wolf-Rayet star surrounded by a planetary nebula with an apparent ring structure. There are many physical similarities between CPD - 56°8032 and He 2-113 such as age, flux and distance. These similarities are reflected in the strong resemblance of their observed spectra and hence they are normally investigated jointly. The observational data of this object were obtained from De Marco *et al* (1997) where 13 lines, given in Table 2, were extracted following a selection process. The  $\chi^2$  plot indicates  $T \simeq 16200$  K which agrees very well with some previously-deduced values notably those of De Marco *et al* (De Marco *et al* 1997; De Marco & Barlow 2001).

## 4 ELECTRON ENERGY DISTRIBUTIONS

It has been suggested (Nicholls *et al* 2012) that the discrepancy between the results of ORLs and those of CELs is based on the assumption of a Maxwell-Boltzmann (M-B) for the electron distribution in the nebulae and that by assuming a different type of distribution, e.g. a  $\kappa$ -distribution, the ORLs and CELs might yield very similar results for the abundance and electron temperature. One way for testing this proposal is to use DR lines to directly sample the distribution and compare to the M-B and other distributions.

The cross-section for dielectronic recombination can be expressed (e.g. Davies & Seaton (1969))

$$\sigma_{\text{DR}} = \frac{\pi}{2} \left( \frac{\hbar}{mv} \right)^2 \frac{\omega_r}{\omega_+} P(\epsilon) \quad (2)$$

where  $P(\epsilon)$  is the dielectronic recombination probability, the probability of capture of a free electron of energy  $\epsilon$  and velocity  $v$  by an ion of statistical weight  $\omega_+$  with the emission of a photon *via* a resonance state of statistical weight  $\omega_r$ ;  $\hbar$  and  $m$  being the reduced Planck's constant and mass of electron respectively. The recombination coefficient for dielectronic recombination *via* the resonance  $r$  is given by

$$\alpha_{\text{DR}} = \int_{\text{res}} \sigma_{\text{DR}} v f(\epsilon) d\epsilon \quad (3)$$

where  $f(\epsilon)$  is the fraction of free electrons per unit energy. So

$$\alpha_{\text{DR}} = \frac{\pi}{2} \frac{\omega_r}{\omega_+} \left( \frac{\hbar}{mv} \right)^2 v_r f(\epsilon_r) \int_{\text{res}} P(\epsilon) d\epsilon \quad (4)$$

where we have assumed that the resonance is narrow compared to changes in  $v$  and  $P(\epsilon)$  so that  $v_r$  and  $\epsilon_r$  are the electron velocity and energy at the resonance position. Several workers have shown (e.g. Bell & Seaton (1985)) that for an isolated narrow resonance

$$\int_{\text{res}} P(\epsilon) d\epsilon = \frac{2\pi\hbar \Gamma^r \Gamma^a}{\Gamma^r + \Gamma^a} \quad (5)$$

where  $\Gamma^r$  and  $\Gamma^a$  are probabilities of radiative decay and autoionisation in units of inverse time. We define a departure coefficient  $b_r$  by

$$b_r = \frac{\Gamma^a}{\Gamma^r + \Gamma^a} \quad (6)$$

which tends to unity for  $\Gamma^a \gg \Gamma^r$ . We have assumed here that only dielectronic capture, autoionisation and radiative

decay determine the population of the autoionising state. In principle there will also be radiative cascading from energetically higher autoionising states. In practice it is negligible for the transitions we consider here. The dielectronic recombination coefficient for a transition of wavelength  $\lambda$  from the resonance state  $r$  is then given by

$$\alpha_{\text{DR}}(\lambda) = 2\pi^2 a_0^3 \frac{\omega_r}{\omega_+} R \left( \frac{R}{\epsilon_r} \right)^{1/2} \Gamma^r(\lambda) b_r f(\epsilon_r) \quad (7)$$

where  $a_0$  is the Bohr radius,  $R$  is the Rydberg constant and where  $\Gamma^r(\lambda)$  is the radiative transition probability corresponding to the line of wavelength  $\lambda$ . The emissivity of a DR line is given by

$$j(\lambda) = \frac{1}{4\pi} N^e N^+ \alpha_{\text{DR}}(\lambda) \frac{hc}{\lambda} \quad (8)$$

where  $N^e$  and  $N^+$  are the number density of electrons and ions respectively,  $h$  is the Planck's constant and  $c$  is the speed of light. Hence we may write for the flux of the transition with wavelength  $\lambda$

$$I(\lambda) = C \frac{\alpha_{\text{DR}}(\lambda)}{\lambda} \quad (9)$$

where  $C$  is a proportionality factor and therefore

$$f(\epsilon_r) = DI(\lambda) \frac{\omega_+}{\omega_r} \left( \frac{\epsilon_r}{R} \right)^{1/2} \frac{\lambda}{\Gamma^r b_r} \quad (10)$$

where  $D$  is another proportionality factor. The observed intensities are taken from Table 2 and the necessary atomic parameters are given in Table 1. Thus for each DR line arising directly from an autoionising state (FF and FB transitions), we can obtain the fraction of free electrons at the energy of that state. The resulting values of  $f(\epsilon)$  can then be compared to various theoretical electron energy distributions.

We derive values of  $f(\epsilon)$  for all the data sets that contain more than one FF or FB transition. In Figures 5-9 the results are presented. In these plots of  $\epsilon^{-1/2} f(\epsilon)$  against  $\epsilon$ , the M-B distribution,

$$f_{\text{MB}}(T, \epsilon) = \frac{2}{(kT)^{3/2}} \sqrt{\frac{\epsilon}{\pi}} e^{-\frac{\epsilon}{kT}} \quad (11)$$

appears as a straight line, where  $k$  is the Boltzmann constant, and  $T$  is the electron temperature shown at the optimum temperature obtained previously.

We also show in these figures non-Maxwellian  $\kappa$ -distributions for comparison, defined by (Bryans 2005)

$$f_{\kappa, \epsilon_\kappa}(\epsilon) = \frac{2}{\sqrt{\pi} \kappa^{3/2} \epsilon_\kappa} \sqrt{\frac{\epsilon}{\epsilon_\kappa}} \frac{\Gamma(\kappa+1)}{\Gamma(\kappa - \frac{1}{2})} \left( 1 + \frac{\epsilon}{\kappa \epsilon_\kappa} \right)^{-(\kappa+1)} \quad (12)$$

where  $\kappa$  is a parameter characterising the distributions, while  $\epsilon_\kappa$  is a characteristic energy. The  $\kappa$ -distributions in these figures were calculated using the best fit temperatures from section 3. We show curves for  $\kappa = 5$  and  $\kappa = 15$ , the former to illustrate clearly how the shape of a  $\kappa$  distribution deviates from M-B in this representation, and the latter as representative of the values proposed by Nicholls *et al* (2012) to resolve the CEL/ORL abundance and temperature problem. In the  $\kappa$ -distribution there are more electrons than M-B at low energies and high energies and fewer at intermediate energies. The deviation of the  $\kappa$ -distribution from M-B increases as  $\kappa$  decreases. In typical nebular conditions the  $\kappa$ -distribution is greater than M-B for energies

greater than 0.25-0.30 Ryd. This energy range is not accessible with the lines and atomic data in use here. The low energy crossover occurs for energies typically below 0.05 Ryd in the Figures shown here. There are three groups of transitions whose upper states lie in this energy region and can therefore potentially determine the shape of the distribution at the lowest energies and differentiate between the different distributions. They are  $3d' \ ^2P^o-3p' \ ^2P^e$ , lines 21–24 in Table 1,  $3d' \ ^2D_{5/2}^o-3p' \ ^2P_{3/2}^e$ , line 38, and  $3d' \ ^2F^o-3p' \ ^2D^e$ , lines 51–53. The transition with the upper state with the lowest energy is line 38 at 6098.51 Å which is only present in the spectrum of IC 418. Indeed all the spectra except IC 418 show only one multiplet in the low energy region, so that the distribution is poorly constrained. However, inspection of Figures 5-7 suggests that, for the planetaries in our sample, the overall curvature of the  $\kappa$ -distributions does not match the observations as well as the M-B distribution. In particular, in the case of IC 418, the object for which the observational data have the greatest number and spread of points, there appears to be significant depletion of electrons at the lowest and highest energies sampled relative to M-B and hence to any  $\kappa$ -distribution.

A more quantitative assessment of the  $\kappa$ -distribution function that best matches the observational data can be obtained by calculating  $\chi^2$  from the derived  $f(\epsilon)$  and the  $\kappa$ -distribution as a function of  $\kappa$ . However, the  $\kappa$ -distribution is also a function of the characteristic energy  $\epsilon_\kappa$  from which we can define a temperature from  $T_\kappa = \epsilon_\kappa/k$  which tends to the M-B temperature as  $\kappa \rightarrow \infty$ . Hence the optimum match of a  $\kappa$ -distribution may not occur at the temperature derived assuming a M-B distribution. Therefore we evaluate  $\chi^2$  as a function of  $1/\kappa$  and  $T_\kappa$  and the results are shown as contour plots in Figures 10-13. The errors on the observational data were derived as described in Section 2.3 above. Figures 10 and 11 show this measure for NGC 7009, the object with the largest ADF and CPD - 56°8032, an object where there is no reason to expect deviations from M-B. Note that in these plots  $1/\kappa = 0$  corresponds to a M-B distribution. Figures 12 and 13 show the  $\chi^2$  distributions for two more planetary nebulae with smaller ADFs than NGC 7009. For these latter two objects, the values of  $\chi^2$  derived using the authors' flux error estimates were unreasonably large, so we have normalised  $\chi^2$  so that the minimum value as a function of  $\kappa$  and  $T_\kappa$  is unity. We omit a contour plot for He 2-113 since it is essentially the same as that for CPD - 56°8032.

The two main features of these four figures are;

(i) The minimum value of  $\chi^2$  occurs for  $1/\kappa = 0$  in all cases, so that the best value of  $T_\kappa = T$ . This is a quantitative reflection of the qualitative observation that the data points suggest negative curvature of  $f(\epsilon)/\sqrt{\epsilon}$  with respect to  $\epsilon$  whereas the M-B distribution has zero curvature and  $\kappa$ -distributions have positive curvature.

(ii) For values of  $T_\kappa$  close to the minimum and  $1/\kappa \neq 0$ ,  $\chi^2$  differs little from its minimum value. Indeed, if we take a change of reduced  $\chi^2$  of unity to estimate the confidence interval on  $\kappa$ , then  $10 \leq \kappa \leq \infty$  is possible in all cases. This is simply a reflection of the magnitude of the uncertainties, both in the observations with the current data sets extracted from the literature and in the calculated atomic parameters.

#### 4.1 Two-component models

Various authors (e.g. Liu *et al* (2000)) have suggested two-component models to explain the ORL/CEL abundance discrepancy, in which a cold metal rich component is embedded in a hotter medium. Suppose a nebula consists of two distinct but individually homogeneous components (1 and 2) in which the electron energy distributions are assumed to be Maxwell-Boltzmann ( $f_{MB}(T, \epsilon)$ ). The components have different electron number densities ( $N_1^e$  and  $N_2^e$ ) and electron temperatures ( $T_1$  and  $T_2$ ) and  $\beta$  is the fraction of the total volume ( $V$ ) occupied by component 1. Then the power radiated in a line at wavelength  $\lambda$  will be given by

$$P_1(\lambda) = V\beta N_1^e N_1^+ \alpha_{DR}(\lambda, T_1) \frac{hc}{\lambda} \quad (13)$$

$$P_2(\lambda) = V(1 - \beta) N_2^e N_2^+ \alpha_{DR}(\lambda, T_2) \frac{hc}{\lambda} \quad (14)$$

where  $N_1^+$  and  $N_2^+$  are the number densities of  $C^{2+}$  in components 1 and 2 respectively. Then adding  $P_1$  and  $P_2$  to get the total power, which is proportional to the observed flux,  $I$ , and using the expression for  $\alpha_{DR}$  in terms of an electron energy distribution, we get

$$\frac{I\lambda}{\omega_r b_r \Gamma^r(\lambda)} \epsilon^{\frac{1}{2}} \propto \beta N_1^e N_1^+ f_{MB}(\epsilon, T_1) + (1 - \beta) N_2^e N_2^+ f_{MB}(\epsilon, T_2) \quad (15)$$

where  $\epsilon$  is now the energy of the resonance which is the upper state of the transition of wavelength  $\lambda$ . To plot the quantity on the RHS we need to relate the number densities in the two component model to those in a single component model for which

$$\frac{I\lambda}{\omega_r b_r \Gamma^r(\lambda)} \epsilon^{\frac{1}{2}} \propto N^e N^+ f_{MB}(\epsilon, T) \quad (16)$$

We require that if  $T_1 = T_2 = T$  the RHS are identical so

$$N^e N^+ = \beta N_1^e N_1^+ + (1 - \beta) N_2^e N_2^+ \quad (17)$$

or

$$(N^e)^2 a = \beta (N_1^e)^2 a_1 + (1 - \beta) (N_2^e)^2 a_2 \quad (18)$$

where the  $a$ 's are the abundances of  $C^{2+}$  relative to  $N^e$  in the various components. The normalised two-component distribution is then

$$\beta \frac{(N_1^e)^2 a_1}{(N^e)^2 a} f_{MB}(\epsilon, T_1) + (1 - \beta) \frac{(N_2^e)^2 a_2}{(N^e)^2 a} f_{MB}(\epsilon, T_2) \quad (19)$$

The constants preceding the MB distribution functions are essentially relative fractional emission measures for the two components.

We construct an illustrative two component model for NGC 7009 based on the model IH2 of Liu *et al* (2000) for NGC 6153, with  $T_1 = 10000$  K,  $T_2 = 500$  K and  $T = 5700$  K from our work. We also assume  $N_1^e = 5000 \text{ cm}^{-3}$ ,  $N_2^e = 1000 \text{ cm}^{-3}$ ,  $a_1/a = 0.6$ ,  $a_2/a = 70$  and  $\beta = 0.7$ . The value of  $a_2 = N(C^{2+})/N_2^e$  is taken from the  $N(O^{2+})/N(H)$  ratio of Liu *et al* (2000) in the metal-rich component of NGC 6153. With these parameters, the normalised two component distribution is

$$0.333 f_{MB}(\epsilon, T_1) + 0.667 f_{MB}(\epsilon, T_2) \quad (20)$$

The resulting distribution is shown in Figure 5. Note that NGC 7009 has a significantly lower ADF (3-9, see Table 3) than NGC 6153 (approximately 10, Liu *et al* (2000)), so



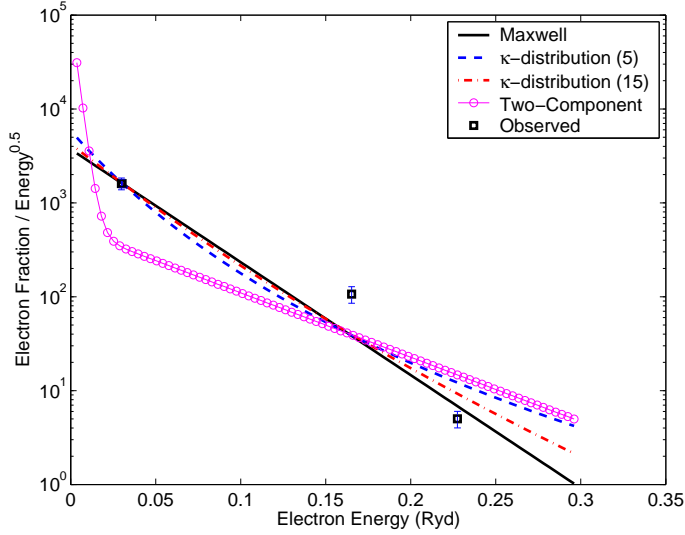


**Figure 5.** Electron distribution plot for the NGC 7009 data of Fang & Liu (2011), showing a Maxwell-Boltzmann and two  $\kappa$ -distributions ( $\kappa = 5.0$  and  $15.0$ ) for  $T = 5700$  K. A two-component Maxwell-Boltzmann distribution with  $T_1 = 10000$  K and  $T_2 = 500$  K is also plotted. The  $y$ -axis has an arbitrary scaling. The factor used to scale the observational data points to the theoretical curves was obtained by minimising the weighted least squares difference between the observational data points and their counterparts on a M-B distribution.

departures from a single temperature model would be expected be less extreme than modelled here. In addition, the emission measures and temperatures of the two components would be expected to differ between the two nebulae. Choosing a higher temperature ( $T_1$ ) and larger emission measure for the low temperature component, for example, would improve the agreement with the low energy data point. Hence plots such as Figure 5 should place significant and useful constraints on the parameters of any two-component model.

## 5 CONCLUSIONS

We have determined an electron temperature from dielectronic recombination lines in a number of astronomical objects, mainly planetary nebulae, by analysing C II transitions which originate from low-lying autoionising states and the subsequent decays. In the analysis we used a least squares minimisation method to find the electron temperature which best fits all the reliable observational data. For the planetary nebulae, our results generally fall below those derived from CELs such as the [O III] forbidden lines and above those from ORLs like the O II permitted lines. There are exceptions however. In NGC 7027, for example, our temperatures broadly confirm the forbidden line results while the O II ORLs yield a much lower temperature. In those objects, which are not planetary nebulae (DQ Her, CPD - 56°8032, and He 2-113), where a similar approach has been used before, we find good agreement with the earlier results. We also find that the theoretical line emissivities that we predict are entirely consistent with those previously published by Davey *et al* (2000) for  $\lambda 4267$ . Given the very different but relatively simple mechanism of formation of the DR lines we

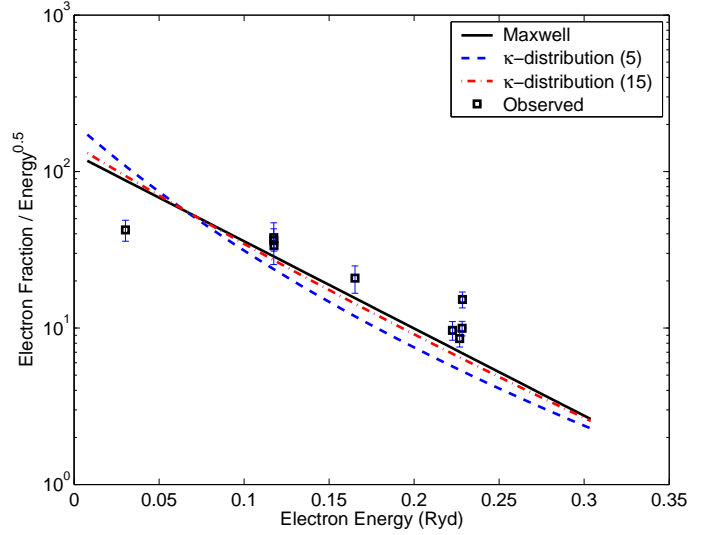


**Figure 6.** Electron distribution plot for NGC 7027 data of Zhang *et al* (2005), showing a Maxwell-Boltzmann and two  $\kappa$ -distributions ( $\kappa = 5.0$  and  $15.0$ ) for  $T = 12300$  K. The  $y$ -axis scaling is as in Figure 5.

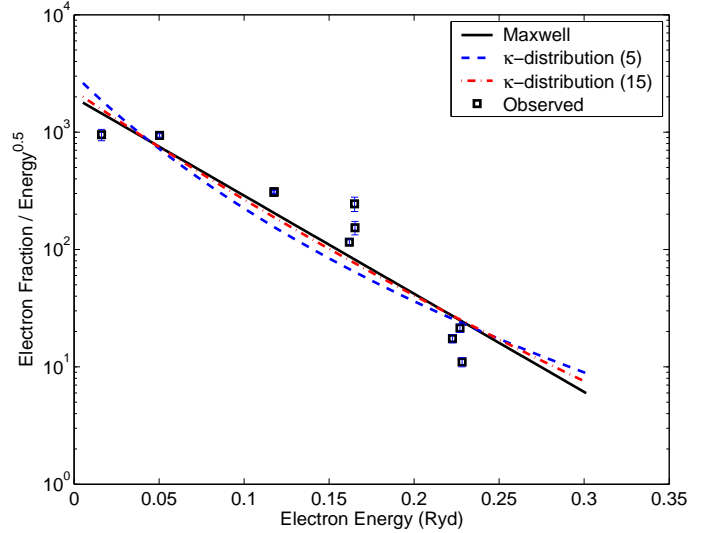


**Figure 7.** Electron distribution plot for IC 418 data of Sharpee *et al* (2003), showing a Maxwell-Boltzmann and two  $\kappa$ -distributions ( $\kappa = 5.0$  and  $15.0$ ) for  $T = 8200$  K. The  $y$ -axis scaling is as in Figure 5.

can conclude that the theoretical emissivities for  $\lambda 4267$  and other similar C II lines are reliable.

We have also proposed and demonstrated a method to test directly whether the free-electron energy distribution in planetary nebulae departs from Maxwell-Boltzmann. We showed that the fluxes of DR lines originating directly from autoionising states can be used to sample the free-electron energy distribution and we applied this method to our sample of objects. We showed that, for all the objects where suitable data are available, a Maxwell-Boltzmann distribution gives the best fit to the observations but that the uncertainties in the observational data and atomic parameters are such that a  $\kappa$ -distribution with values of  $\kappa$  as sug-



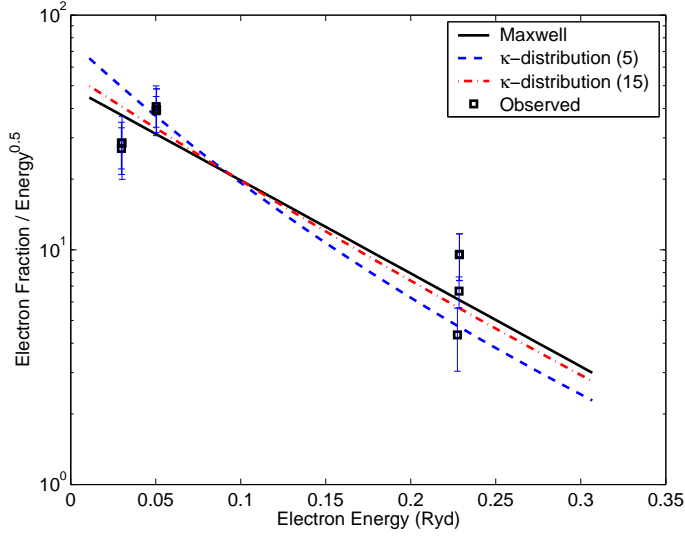


**Figure 8.** Electron distribution plot for CPD - 56°8032 data of De Marco *et al* (1997), showing a Maxwell-Boltzmann and two  $\kappa$ -distributions ( $\kappa = 5.0$  and  $15.0$ ) for  $T = 17300$  K. The  $y$ -axis scaling is as in Figure 5.

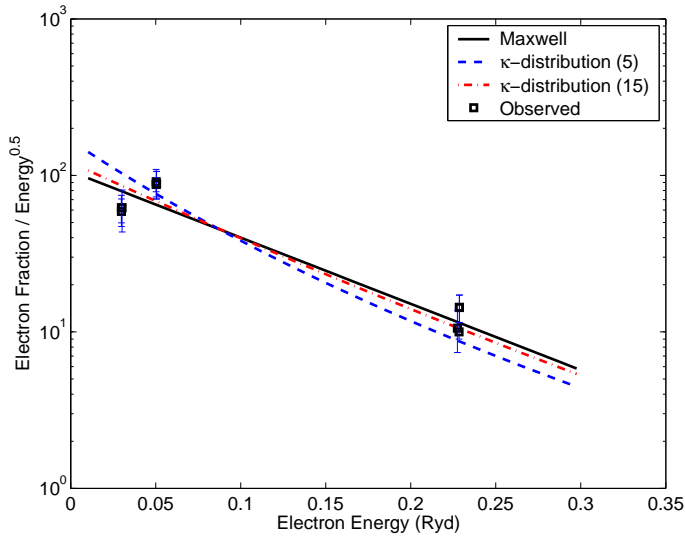


**Figure 9.** Electron distribution plot for He 2-113 data of De Marco *et al* (1997), showing a Maxwell-Boltzmann and two  $\kappa$ -distributions ( $\kappa = 5.0$  and  $15.0$ ) for  $T = 16200$  K. The  $y$ -axis scaling is as in Figure 5.

gested by Nicholls *et al* (2012) is not excluded. Similarly a two-component model as described by Liu *et al* (2000) for NGC 6153 is also not excluded, although significant constraints are imposed on any such model by the DR lines. We have highlighted several spectral lines which make it possible to sample the low energy part of the electron energy distribution where departures from a simple one-component Maxwell-Boltzmann distribution are expected. Higher precision is needed in the measurement of the intensities of these lines to fully realise the potential of this method.

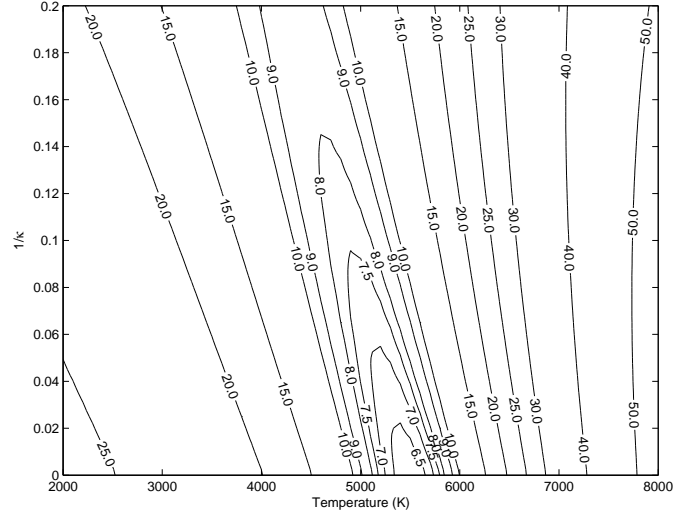


**Figure 10.**  $\chi^2$  derived from the difference between  $f(\epsilon)$  and a  $\kappa$ -distribution as a function of  $1/\kappa$  and  $T_\kappa$  for NGC 7009.

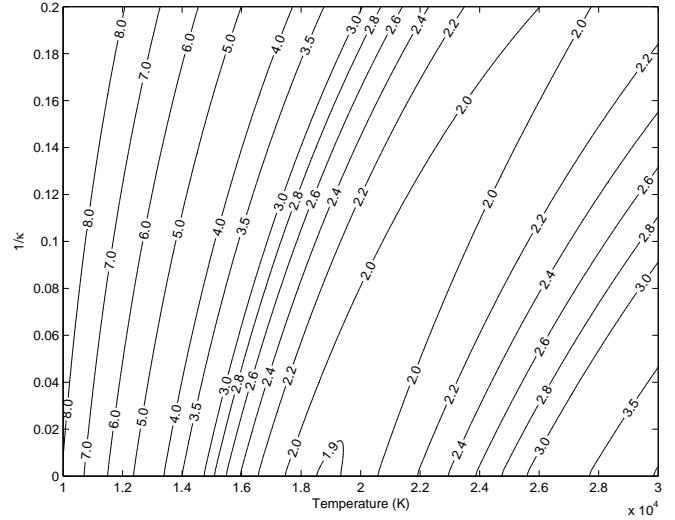


**Figure 11.**  $\chi^2$  derived from the difference between  $f(\epsilon)$  and a  $\kappa$ -distribution as a function of  $1/\kappa$  and  $T_\kappa$  for CPD - 56°8032.

## REFERENCES

- Baluteau J.P., Zavagno A., Morisset C., Péquignot D., 1995, *A&A*, 303, 175
- Barlow M.J., Hales A.S., Storey P.J., Liu X.-W., Tsamis Y.G., Aderin M.E., 2006, *International Astronomical Union (Symposium S234)*, 2, 367
- Bell R.H., Seaton M.J., 1985, *J. Phys. B*, 18, 1589
- Berrington K.A., Eissner W.B., Norrington P.H., 1995, *Comput. Phys. Communications*, 92, 290
- Bryans P., 2005, PhD thesis, University of Strathclyde
- Davey A.R., 1995, PhD thesis, University College London
- Davey A.R., Storey P.J., Kisielius R., 2000, *A&AS*, 142, 85
- Davies P.C.W., Seaton M.J., 1969, *ApJ*, 2, 757
- De Marco O., Barlow M.J., Storey P.J., 1996, *Astrophys Space Sci*, 238, 91
- De Marco O., Storey P.J., Barlow M.J., 1996, *ASP Conference Series*, 96, 145

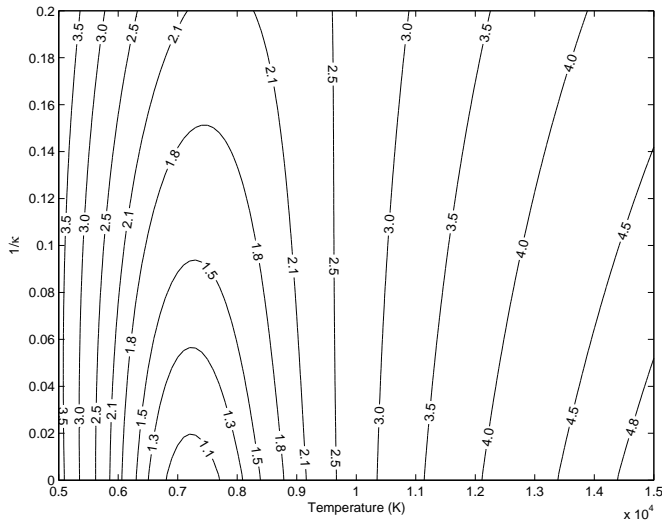


**Figure 12.**  $\chi^2$  derived from the difference between  $f(\epsilon)$  and a  $\kappa$ -distribution as a function of  $1/\kappa$  and  $T_\kappa$  for IC 418.

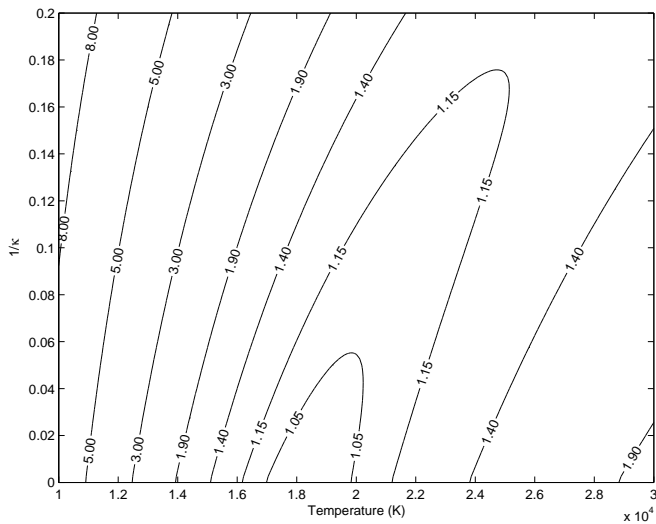


**Figure 13.**  $\chi^2$  derived from the difference between  $f(\epsilon)$  and a  $\kappa$ -distribution as a function of  $1/\kappa$  and  $T_\kappa$  for NGC 7027.

- Liu X.-W., Storey P.J., Barlow M.J., Danziger I.J., Cohen M., Bryce M., 2000, MNRAS, 312, 585
- Liu X.-W., 2002, RevMexAA, 12, 70
- Liu Y., Liu X.-W., Barlow M.J., Luo S.-G., 2004, MNRAS, 353, 1251
- Liu X.-W., Barlow M.J., Zhang Y., Bastin R.J., Storey P.J., 2006, MNRAS, 368, 1959
- Liu X.-W., 2006, International Astronomical Union (Symposium S234), 2, 219
- Nicholls D.C., Dopita M.A., Sutherland R.S., 2012, ApJ, 752, 148
- Nussbaumer H., Storey P.J., 1978, A&A, 64, 139
- Peimbert M., Peimbert A., Ruiz M.T., Esteban C., 2004, ApJS, 150, 431
- Sharpee B., Williams R., Baldwin J.A., van Hoof P.A.M., 2003, ApJS, 149, 157
- Smits D.P., 1991, MNRAS, 248, 193
- Sochi T., 2010, Communications in Computational Physics, 7, 1118
- Sochi T., Storey P.J., 2012, Atomic Data and Nuclear Data Tables, (Accepted)
- Sochi T., 2012, PhD thesis, University College London
- Tsamis Y.G., Barlow M.J., Liu X.-W., Danziger I.J., Storey P.J., 2003, MNRAS, 338, 687
- Tsamis Y.G., Barlow M.J., Liu X.-W., Storey P.J., Danziger I.J., 2004, MNRAS, 353, 953
- Tsamis Y.G., Walsh J.R., Péquignot D., Barlow M.J., Liu X.-W., Danziger I.J., 2007, The Messenger, 127, 53
- Tsamis Y.G., Walsh J.R., Péquignot D., Barlow M.J., Danziger I.J., Liu X.-W., 2008, MNRAS, 386, 22
- Wang W., Liu X.-W., 2007, MNRAS, 381, 669
- Zhang Y., Liu X.-W., Luo S.-G., Péquignot D., Barlow M.J., 2005, A&A, 442, 249

- De Marco O., Storey P.J., Barlow M.J., 1997, MNRAS, 297, 999
- De Marco O., Barlow M.J., 2001, Astrophys Space Sci, 275, 53
- Eissner W., Jones M., Nussbaumer H., 1974, Comput. Phys. Communications, 8, 270
- Fang X., Liu X.-W., 2011, MNRAS, 415, 181
- Ferland G.J., Williams R.E., Lambert D.L., Shields G.A., Slovak M., Gondhalekar P.M., Truran J.W., 1984, ApJ, 281, 194
- García-Rojas J.; Esteban C., 2007, ApJ, 670, 457
- García-Rojas J., Pena M., Peimbert A., 2009, A&A, 496, 139
- Garnett D.R., Dinerstein H.L., 2001, RevMexAA, 10, 13
- Kholtygin A.F., 1998, A&A, 329, 691
- Liu X.-W., Storey P.J., Barlow M.J., Clegg R.E.S., 1995, MNRAS, 272, 369

Table 1: Observed transitions used in the current study where the columns stand for: an arbitrary transition index, the wavelength in Å, the lower level designation and its statistical weight, the upper level designation and its statistical weight, transition status (FF, FB or BB), the radiative transition probability in  $s^{-1}$ , the departure coefficient of the upper autoionising state in the case of FF and FB transitions and its energy in Ryd above the  $C^{2+} 1s^2 2s^2 1S^e$  ionisation threshold. The wavelengths are given as the vacuum's for  $\lambda < 2000$  Å and as the air's for  $\lambda > 2000$  Å. The prime in the level designation indicates an excited core, i.e.  $1s^2 2s 2p(^3P^o)$ , and the  $1s^2$  core is suppressed from all other configurations.

In.	$\lambda$	L	$\omega_l$	U	$\omega_u$	St.	$\Gamma_{ul}^r(\lambda)$	$b_u$	$\epsilon_u$
1	1334.53	$2s^2 2p^2 P^o$	2	$2s 2p^2^2 D^e$	4	BB	2.403E+8		
2	1335.66	$2s^2 2p^2 P^o$	4	$2s 2p^2^2 D^e$	4	BB	4.753E+7		
3	1335.71	$2s^2 2p^2 P^o$	4	$2s 2p^2^2 D^e$	6	BB	2.869E+8		
4	3588.91	$3p' ^4 D^e$	2	$4s' ^4 P^o$	2	FB	4.920E+7	0.9062	0.117441
5	3590.76	$3p' ^4 D^e$	4	$4s' ^4 P^o$	2	FB	4.945E+7	0.9062	0.117441
6	3590.88	$3p' ^4 D^e$	6	$4s' ^4 P^o$	4	FB	6.232E+7	0.9595	0.117661
7	3876.19	$3d' ^4 F^o$	10	$4f' ^4 G^e$	12	FB	2.629E+8	0.0000	0.227272
8	3876.39	$3d' ^4 F^o$	8	$4f' ^4 G^e$	10	FB	2.296E+8	0.3399	0.227005
9	3876.65	$3d' ^4 F^o$	6	$4f' ^4 G^e$	8	FB	2.116E+8	0.3627	0.226808
10	4267.00	$2s^2 3d^2 D^e$	4	$2s^2 4f^2 F^o$	6	BB	2.185E+8		
11	4267.26	$2s^2 3d^2 D^e$	6	$2s^2 4f^2 F^o$	8	BB	2.340E+8		
12	4267.26	$2s^2 3d^2 D^e$	6	$2s^2 4f^2 F^o$	6	BB	1.560E+7		
13	4318.61	$3p' ^4 P^e$	2	$4s' ^4 P^o$	4	FB	3.470E+7	0.9595	0.117661
14	4323.11	$3p' ^4 P^e$	2	$4s' ^4 P^o$	2	FB	1.374E+7	0.9062	0.117441
15	4372.38	$3d' ^4 P^o$	4	$4f' ^4 D^e$	4	FF	9.895E+7	0.9846	0.228409
16	4376.58	$3d' ^4 P^o$	4	$4f' ^4 D^e$	6	FF	1.189E+8	0.9952	0.228209
17	4411.15	$3d' ^2 D^o$	4	$4f' ^2 F^e$	6	FF	1.855E+8	0.4063	0.222570
18	4618.56	$3d' ^2 F^o$	6	$4f' ^2 G^e$	8	FF	1.931E+8	0.6893	0.227110
19	4619.25	$3d' ^2 F^o$	8	$4f' ^2 G^e$	10	FF	2.288E+8	0.7843	0.227462
20	4627.50	$3d' ^2 F^o$	8	$4f' ^2 G^e$	8	FF	9.390E+6	0.6893	0.227110
21	4953.86	$3p' ^2 P^e$	2	$3d' ^2 P^o$	2	FB	2.469E+7	0.9929	0.050483
22	4958.66	$3p' ^2 P^e$	4	$3d' ^2 P^o$	2	FB	1.240E+7	0.9929	0.050483
23	4959.92	$3p' ^2 P^e$	2	$3d' ^2 P^o$	4	FB	6.017E+6	0.9925	0.050258
24	4964.74	$3p' ^2 P^e$	4	$3d' ^2 P^o$	4	FB	3.135E+7	0.9925	0.050258
25	5107.81	$3d' ^2 P^o$	4	$4f' ^2 D^e$	4	FF	2.158E+7	0.9985	0.228615
26	5113.65	$3d' ^2 P^o$	4	$4f' ^2 D^e$	6	FF	1.185E+8	0.9979	0.228411
27	5114.26	$3d' ^2 P^o$	2	$4f' ^2 D^e$	4	FF	1.060E+8	0.9985	0.228615
28	5132.95	$3s' ^4 P^o$	2	$3p' ^4 P^e$	4	BB	3.704E+7		
29	5133.28	$3s' ^4 P^o$	4	$3p' ^4 P^e$	6	BB	2.700E+7		
30	5143.49	$3s' ^4 P^o$	4	$3p' ^4 P^e$	2	BB	7.550E+7		
31	5145.16	$3s' ^4 P^o$	6	$3p' ^4 P^e$	6	BB	6.354E+7		
32	5151.08	$3s' ^4 P^o$	6	$3p' ^4 P^e$	4	BB	4.176E+7		
33	5259.06	$3d' ^4 F^o$	8	$4p' ^4 D^e$	6	FB	2.063E+7	0.9576	0.165218
34	5259.66	$3d' ^4 F^o$	4	$4p' ^4 D^e$	2	FB	2.482E+7	0.0167	0.164896
35	5259.76	$3d' ^4 F^o$	6	$4p' ^4 D^e$	4	FB	2.010E+7	0.9429	0.165014
36	5485.91	$3d' ^4 D^o$	6	$4p' ^4 D^e$	6	FB	3.323E+6	0.9576	0.165218
37	5648.07	$3s' ^4 P^o$	4	$3p' ^4 S^e$	4	BB	1.945E+7		
38	6098.51	$3p' ^2 P^e$	4	$3d' ^2 D^o$	6	FB	5.026E+7	0.0261	0.016144
39	6250.76	$3d' ^2 D^o$	6	$4p' ^2 P^e$	4	FF	2.733E+7	0.8281	0.161889
40	6779.94	$3s' ^4 P^o$	4	$3p' ^4 D^e$	6	BB	2.497E+7		
41	6780.59	$3s' ^4 P^o$	2	$3p' ^4 D^e$	4	BB	1.486E+7		
42	6783.91	$3s' ^4 P^o$	6	$3p' ^4 D^e$	8	BB	3.542E+7		
43	6787.21	$3s' ^4 P^o$	2	$3p' ^4 D^e$	2	BB	2.946E+7		
44	6791.47	$3s' ^4 P^o$	4	$3p' ^4 D^e$	4	BB	1.875E+7		
45	6798.10	$3s' ^4 P^o$	4	$3p' ^4 D^e$	2	BB	5.803E+6		
46	6800.69	$3s' ^4 P^o$	6	$3p' ^4 D^e$	6	BB	1.042E+7		
47	6812.28	$3s' ^4 P^o$	6	$3p' ^4 D^e$	4	BB	1.708E+6		
48	7112.48	$3p' ^4 D^e$	2	$3d' ^4 F^o$	4	BB	3.321E+7		
49	7113.04	$3p' ^4 D^e$	4	$3d' ^4 F^o$	6	BB	3.558E+7		
50	7115.63	$3p' ^4 D^e$	6	$3d' ^4 F^o$	8	BB	4.062E+7		
51	8794.08	$3p' ^2 D^e$	6	$3d' ^2 F^o$	8	FB	2.034E+7	0.9982	0.030241
52	8800.28	$3p' ^2 D^e$	4	$3d' ^2 F^o$	6	FB	1.897E+7	0.9981	0.029860
53	8826.55	$3p' ^2 D^e$	6	$3d' ^2 F^o$	6	FB	1.405E+6	0.9981	0.029860

Table 2: The observed flux data for the investigated objects where the first column is the index as given in Table 1, while the other columns give the investigated objects. For NGC 7027, the first column belongs to the data of Baluteau *et al* (1995) and the second to the data of Zhang *et al* (2005). For NGC 2867, the first value is related to knot 1 and the second to knot 2. The given flux is the value normalised to  $H\beta = 100$  value except for the CPD - 56°8032 and He 2-113 where it is given as the absolute value in units of  $\text{erg.s}^{-1}.\text{cm}^{-2}$  and in multiples of  $10^{-12}$ . The symbol ‘xx’ indicates that the previous value of flux in that column is shared by the indicated lines in that multiplet.

In.	NGC 7009	NGC 5315	NGC 7027	NGC 7027	IC 418	NGC 2867	DQ Her	CPD 56°8032	He 2-113
1							270		
2							xx		
3							xx		
4				0.018					
5				0.059	0.0252				
6				xx	xx				
7					0.0069				
8					xx				
9				0.026	xx				
10	0.8795	0.6559		0.575	0.5712	0.814(1.246)	29		
11	xx	xx		xx	xx	xx	xx		
12	xx	xx		xx	xx	xx	xx		
13					0.0086				
14				0.004					
15				0.026					
16				0.031	0.0016				
17				0.019	0.0016				
18	0.0021			0.009				4.1940	2.2710
19	0.0021							6.1670	3.3390
20								0.1850	0.1002
21								1.4370	0.7141
22								0.7183	0.3571
23								0.7183	0.3571
24					0.0211			3.5920	1.7850
25								0.5906	0.1973
26								3.3840	1.1300
27								2.8880	0.9646
28	0.0088				0.0044				
29				0.013	xx				
30				0.013					
31		0.0039			0.0040				
32				0.009	0.0046				
33				0.009	0.0031				
34					0.0032				
35					xx				
36	0.0004								
37					0.0014				
38					0.0011				
39					0.0015				
40			11.8	0.034	0.0109	0.045(0.079)			
41	0.0070				0.0055				
42			2.1	0.004	0.0022				
43	0.0052		3.7	0.008					
44		0.0068	4.9	0.012	0.0066				
45			0.7						
46		0.0028		0.009	0.0050				
47			0.5	0.001					
48			4.7						
49			xx		0.0052				
50					0.0043				
51	0.0320		11.8	0.015				1.9260	0.9342
52	0.0224							1.3470	0.6533
53								0.0943	0.0457

Table 3: The range of electron temperature, from ORLs and a sample of CELs, in Kelvin, derived from different species and transitions, of the investigated astronomical objects as obtained from the literature where BD stands for Balmer Discontinuity, PD for Paschen Discontinuity, and RF for Radio Frequency. The value in the first row of each type of transition represents the minimum and the second is the maximum. Our results, as derived in the current paper, are given as averages in the additional three rows of C II where the optimal value is in the first row, while the lower and upper limits of the confidence interval are in the second and third rows respectively. Our first value for NGC 7027 belongs to the data of Baluteau *et al* (1995) while the second belongs to the data of Zhang *et al* (2005). Similarly, the two values for NGC 2867 correspond to the first and second knots respectively. In the last row of the table, the range of the abundance discrepancy factor (ADF) values of some of the investigated objects as found in the literature is given. More details about the temperature data and their references can be found in Sochi (2012).

Object	NGC 7009	NGC 5315	NGC 7027	IC 418	NGC 2867	DQ Her	CPD 56°8032	He 2-113
H I(BD)	7200 8150	8600 8600	8000 12800	>15000	8950 8950	450 1000		
H I(PD)	5800 5800		8000 8000					
He I	5040 8000	10000 10000	8200 10360	9800 9800	10250 10900		20100 20100	
C II				9600 9600		700 1450	12800 21700	13600 17000
This work								
$T_{\text{opt}}$	5650	6950	11100(12250)	8200	14300(16000)	1600	17300	16200
$T_{\text{min}}$	4830	4620	9930(8590)	7250	12120(13090)	1460	14020	13630
$T_{\text{max}}$	6240	11990	12660(23180)	9630	17600(26560)	1740	23680	20740
[N II]	10800 11040	9090 10800	12300 12300	8200 9600	8800 11750	2400 2500	11000 11000	
O II	1600 1600	4350 8100	7100 7100					
[O III]	8350 10380	7800 18500	9260 14850	7000 11200	10520 11850			
[N II]+[O III]					11600 11850			
RF				6600 23000				
ADF	3.0-9.10 <sup>a</sup>	1.2-3.4 <sup>b</sup>	1.8 <sup>c</sup>		1.49-1.77 <sup>d</sup>			

<sup>a</sup> Obtained from Liu *et al* (2004); Tsamis *et al* (2004); Liu *et al* (2006); Barlow *et al* (2006); Liu (2006); Wang & Liu (2007); Tsamis *et al* (2008).

<sup>b</sup> Obtained from Tsamis *et al* (2004); García-Rojas & Esteban (2007).

<sup>c</sup> Obtained from Liu *et al* (2004).

<sup>d</sup> Obtained from García-Rojas *et al* (2009).